Carbon 95 (2015) 833–842

Contents lists available at ScienceDirect

Carbon

journal homepage: www.elsevier.com/locate/carbon

Charge carrier transport and separation in pristine and nitrogen-doped graphene nanowiggle heterostructures

Aurélien Lherbier [a, *], Liangbo Liang [b, c], Jean-Christophe Charlier [a], Vincent Meunier [b, d]

[a] Université catholique de Louvain (UCL), Institute of Condensed Matter and Nanosciences (IMCN), 1348 Louvain-la-Neuve, Belgium
[b] Department of Physics, Applied Physics, and Astronomy, Rensselaer Polytechnic Institute, Troy, NY 12180, USA
[c] Center for Nanophase Materials Sciences, Oak Ridge National Laboratory, Oak Ridge, TN 37831, USA
[d] Department of Materials Science and Engineering, Rensselaer Polytechnic Institute, Troy, NY 12180, USA

ARTICLE INFO

Article history:
Received 23 June 2015
Received in revised form
28 August 2015
Accepted 29 August 2015
Available online 3 September 2015

ABSTRACT

Electronic structure methods are combined into a multiscale framework to investigate the electronic transport properties of recently synthesized pristine and nitrogen-doped graphene nanowiggles and their heterojunctions deposited on a substrate. Real-space Kubo-Greenwood transport calculations reveal that charge carrier mobilities reach values up to 1000 $cm^2\ V^{-1}\ s^{-1}$ as long as the amount of substrate impurities is sufficiently low. Owing to their type-II band alignment, atomically precise heterostructures between pristine and N-doped graphene nanowiggles are predicted to be excellent candidates for charge carrier separation devices with potential in photoelectric and photocatalytic water splitting applications.

1. Introduction

Charge carrier mobility is a key parameter in the performance of electronic devices. In that respect, sp^2 carbon-based materials are known for their exceptionally high promises. Intercalated graphite, carbon nanotubes and mono-, or few-, layer graphene are only a few selected examples in the broad family of sp^2 carbon-based structures [1,2]. One major problem with the deployment of sp^2 carbon nanostructures into practical devices is the lack of control of their semiconducting properties, including their electronic band gap. For instance, carbon nanotubes come in a variety of chiralities and can be either semimetallic or semiconducting, with an electronic gap inversely proportional to their diameter [3]. However, despite recent efforts [4], it remains extremely challenging to grow, or to select after growth, a sharp distribution of carbon nanotube types. Furthermore, graphene is semimetallic and the absence of a band gap is a serious drawback for the development of graphene-based logic devices with switching capabilities. These difficulties highlight the importance of selecting graphene-derived materials displaying a practical electronic band gap.

One possible route to resolve this conundrum is to control spatial confinement to the electronic degrees of freedom by reducing the dimensionality from 2D graphene sheets into 1D graphene nanoribbons [5]. However, electronic transport properties of 1D systems are known to be extremely sensitive to disorder, as stated notably by the theory of localization [6]. Care must therefore be taken since there would be no gain in opening a band gap if mobilities were dramatically affected at the same time. Therefore, the constriction of graphene into 1D ribbons requires to carefully maintain a high structural quality.

In this context, a notable breakthrough has been achieved with the development of bottom-up chemistry approaches, where perfectly edged graphene nanoribbons are obtained from the assembly of small monomers [7–11]. The monomers are gradually assembled by chemical reaction and thermal treatment to first form polymers on a metallic surface by Ullmann coupling followed by cyclo-dehydrogenation to yield the coveted atomically sharp graphene ribbons. The method has shown promising versatility since monomers of various shapes, sizes and compositions can be employed to produce different types of ribbons [7,12,13]. These include graphene nanowiggles, which are ribbons with chevron-like edges [14]. The possibility of assembling larger molecules into wider nanoribbons has also been demonstrated, allowing for a fine tuning of the band gap with the change of the nanoribbon width [9,10,13]. The particular case of graphene nanowiggles has been thoroughly investigated to unveil an unprecedented richness of electronic, magnetic, and thermal properties depending on the combination of edge types [14–17].

In addition to pure hydrocarbon monomers, monomers where a

* Corresponding author.
E-mail address: aurelien.lherbier@uclouvain.be (A. Lherbier).

http://dx.doi.org/10.1016/j.carbon.2015.08.111
0008-6223/

number of carbon atoms are substituted by chemical elements such as B or N can also be employed to create atomically precise doped nanoribbons. For instance, nitrogen substitution in the tetraphenyltriphenylene monomers leads to the fabrication of N-doped graphene nanowiggles [18–20]. Such a doping scheme offers opportunities toward an atomic-level control of dopant positions and concentrations in 1D sp^2 carbon materials. A perfect knowledge of the nitrogen dopant positions in the graphene sublattice is expected to yield a number of well-defined features in the materials' electronic spectrum [21–25]. Moreover, a recent work by Cai et al. [20] showed that pristine and substituted monomers can be used concurrently to produce one of the first atomically-sharp carbon-based heterojunctions.

In this work we focus on the intrinsic properties of the type of heterostructures developed by Cai et al., in 2014. We specifically investigate the electronic properties of pristine and N-doped armchair–armchair (AA-) graphene nanowiggles (GNWs) and their heterojunctions using a combination of density functional theory (DFT) and semi-empirical tight-binding (TB) techniques. We first develop a reliable TB parametrization of the pristine and doped GNWs based on the DFT results to study the electronic transport in two types of GNW heterostructures at micrometer scale. Such size upscaling is made possible within the real-space Kubo-Greenwood formalism. The first system under consideration consists of a pristine GNW with random inclusions of N-doped GNW segments. The second system is a long GNW with a single sharp junction between a pristine and a N-doped region deposited on a substrate containing charge impurities. Finally, the potential of such heterostructured GNWs for charge separation devices in particular for photocatalytic water splitting and photoelectric application is discussed.

2. Electronic structure of pristine and N-doped AA-GNWs

2.1. First principles calculations

Density functional theory (DFT), as implemented in SIESTA [26] and VASP [27,28] packages (see Method section for computational details), was employed to compute the electronic band structures and density of states (DOS) of the pristine and nitrogen-doped AA-GNWs. The selected systems correspond to those that were recently experimentally realized [18–20]. Let us first introduce the notation adopted here for the doping scheme: a monomer where n carbon atoms are substituted with n nitrogen atoms is labeled Nn monomer, and the corresponding assembled GNW is likewise denoted as Nn GNW [25], as shown in Fig. 1. Only the results based on the SIESTA package are presented in Fig. 1 (d–f) (black thick lines), since a good agreement for the electronic structures was obtained with both DFT codes.

As shown by the computed electronic band structure diagrams (Fig. 1(d–f) left panels), the three systems have a direct band gap of similar size, i.e., 1.610, 1.613, and 1.540 eV for the pristine, N2 and N4 GNWs respectively. It is important to note that DFT typically underestimates fundamental band gap values. More sophisticated treatments, such as the use of many-body *GW* approach for quasiparticle correction and the image charge model for substrate polarization-induced gap reduction, provide fundamental band gap values in the 2.0–2.8 eV range [25,29–32], in much better agreement with experiments. Note that different experimental works reported different fundamental gap values: some reported ~2.8–3.1 eV [10,18] while others measured ~2.0 eV gaps [20,33]. The origins of these discrepancies can partially be traced back to substrate polarization effects. Although the band gaps are underestimated by DFT, a scissor-type correction can be applied to the presented results without modifying the conclusions on transport properties since the dispersion and overall shape are not significantly affected by the underestimated band gap [34,35]. Overall, the band structure of the AA-GNWs are characterized by pairs of electronic bands separated by small gaps. Interestingly, the pristine and N2 GNWs have almost exactly the same electronic structure, especially for the first two pairs of valence and conduction bands located within the −1.5–1.5 eV energy window. A more pronounced difference appears for the third group of valence and conduction bands. However, as indicated by blue arrows in Fig. 1(e), a clear distinction between these two systems is the presence of two pairs of superimposed flat bands at energies −1.57 eV and −1.66 eV in the case of the N2 GNW. These flat bands correspond to the lone electron pairs localized at the non-hydrogenated nitrogen edge atoms (blue atoms in Fig. 1(b)). These lone electron pairs are strongly localized, as further shown by the non-dispersive character of the corresponding bands. In addition, these electrons do not interact significantly with the rest of the electronic structure and are therefore not appreciably hybridized with the π electronic cloud. This feature is even more pronounced in the N4 GNW system (see Fig. 1(f)), for which these flat bands lie at an energy (−1.30 eV) where dispersive π valence bands are present, without being hybridized. Apart from the position in energy of these flat bands, the main difference between N2 and N4 GNW electronic band structures is observed at about 4/5 of the $\Gamma - X$ line. Around this k point the first two pairs of valence (conduction) bands join (repeal) each others in the case of N4 GNW. The density of states (DOS) corresponding to these band structures is displayed in the central panels of Fig. 1(d–f). A series of van Hove singularities are obtained at the band edges, as expected for 1D systems. Another set of sharp peaks are also observed for energies corresponding to the isolated lone pairs of electrons in case of the N2 and N4 GNWs.

2.2. Parameterized tight-binding calculations

In order to study mesoscopic-sized systems, we developed a single-band tight-binding (TB) model that reproduces the DFT electronic structure of the three types of AA-GNWs mentioned above (See Method section for details). The corresponding TB band structures and DOS are plotted in thin red lines on top of the DFT results in Fig. 1(d–f). An overall good agreement is obtained between TB and DFT electronic structure, in particular for the first two pairs of valence and conduction bands. We also note that depending on the system, the third group of valence and conduction bands is not always accurately reproduced. This is not surprising since our single-band tight-binding model is not expected to represent states that have a significant *s* character. In spite of this, it is justified to use a TB model that accurately represents the properties in an energy windows of ±1 eV since we focus on relatively low-energy transport properties around the top of valence and bottom of conduction bands. This is justified by the fact that in actual transport experiments, the gate voltages (and gate capacitance) hardly allow electrons and holes to reach energies outside a window of ±1 eV with respect to the Fermi level. Therefore in the present case, the transport properties will be dominated by the two first groups of valence and conduction bands. The flat bands corresponding to the lone pairs of electrons ascribed to the nitrogen atoms, are not reproduced by the TB model (Fig. 1(e–f)), since the TB model only accounts for π electrons. However, as discussed earlier, these electronic states do not mix with other electronic states and do not contribute to charge transport since they have a vanishing group velocity.

3. Electronic structure of AA-GNW heterostructures

It has been experimentally shown possible to mix monomers with different compositions to fabricate long GNWs containing

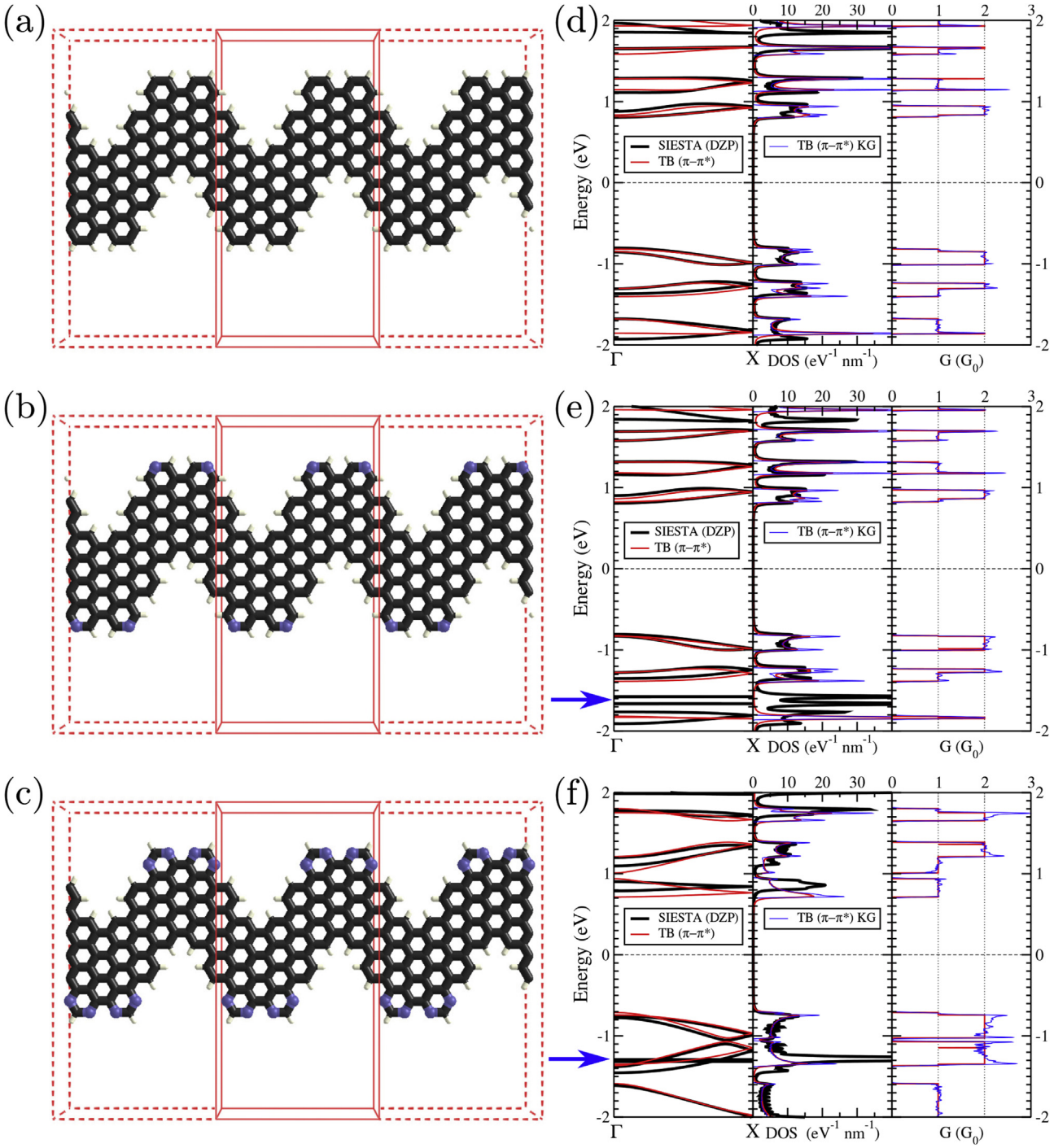

Fig. 1. (a–c) Unit cells (with one repetition on each side) of the three experimentally available GNWs, i.e. pristine, N2 and N4 nitrogen-doped GNWs. (d–f) Corresponding electronic band structure diagrams, density of states obtained by DFT (SIESTA) (black lines) and TB (red lines) calculations, and ballistic conductance plateaus either computed from the GNW unit cell or using the TB-based Kubo-Greenwood (KG) transport approach on 1 μm long GNWs (blues lines). (A colour version of this figure can be viewed online.)

both pristine and N-doped segments [20]. Despite the current lack of full control on the segment size, it is expected that this new technique will be optimized to afford more control on the junction composition. It is therefore relevant to investigate the electronic properties of heterostructures composed of pristine and N-doped AA-GNWs. Of particular importance is the knowledge of the type of band alignment that develops at the interface of the heterostructures. Although the electronic structures of the three types of GNWs studied in the previous section are very similar due in part to the isoelectronicity of the nitrogen atoms and the singly-hydrogenated edge carbon atoms, the presence of lone pairs of electrons is anticipated to induce band offsets in the heterostructures, since they are expected to modify the electronic work-function compared to pristine segments [18,25,36].

In the following, we will only consider the case of heterostructures composed of pristine and N2 GNWs. The band offset is evaluated through the calculation of projected DOS (PDOS). The PDOS is computed for each unit cells constituting the

heterostructure. This enables the determination of which part of the heterostructure, especially at the interface, is responsible for the presence of electronic states in a given window of energy. The considered heterostructure is composed by seven pristine GNW and seven N2 GNW unit cells placed alternatively (Fig. 2). The cells are labeled $p_{i=1,7}$ and $N_{i=1,7}$ for the pristine and N2 regions, respectively. Fig. 2 shows that the electronic bands of the N2 GNW region are down-shifted in energy compared to the ones of the pristine region. Since the structure is periodic, the actual system presents two distinct interfaces, i.e. one between p_1 and N_1, and one between p_7 and N_7. This explains why the PDOS of p_1 (N_1) is identical to the PDOS of p_7 (N_7). The valence and conduction band offsets are thus evaluated from the difference in energy position of the PDOS between p_4 and N_4 regions, i.e., $E_v^{\text{offset}} = 0.32$ eV and $E_c^{\text{offset}} = 0.30$ eV respectively. The PDOS of the *bulk* regions, away from the interface, i.e. from p_2 (N_2) to p_6 (N_6), are almost identical, thereby demonstrating that the interface region is confined quasi entirely within one unit cell on each side. Such a very short interface region has been shown to yield high electric field (~0.2 V nm^{-1}) amenable to charge carrier separation [20]. In the interface region, the PDOS shows important variations and notably presents additional states marked by purple arrows in Fig. 2. In order to compute electronic transport in micrometer long GNWs containing such interfaces between pristine and N2 segments, it is necessary to account for the observed band offset within the TB model. This is achieved by considering an electrostatic potential V_{el} inside the N2 regions. The associated potential energy is modeled by a position-dependent shift of the onsite energies. The application of a potential energy well of $U_{el} = -0.28$ eV on all the atoms of the N2 region yields good agreement between DFT and TB PDOS (Fig. 2).

4. Transport properties in AA-GNWs with random inclusion of N2 segments

The electronic transport properties of long AA-GNWs are now studied using the well-tested semi-empirical TB model presented in the previous section. The structure consists of a pristine GNW where segments of five to sixteen unit cells (ranging from 8.5 to 27.3 nm) are randomly substituted by N2 GNW unit cells (Fig. 3). The AA-GNW contains 1000 unit cells, i.e., a 1.7 μm long structure.

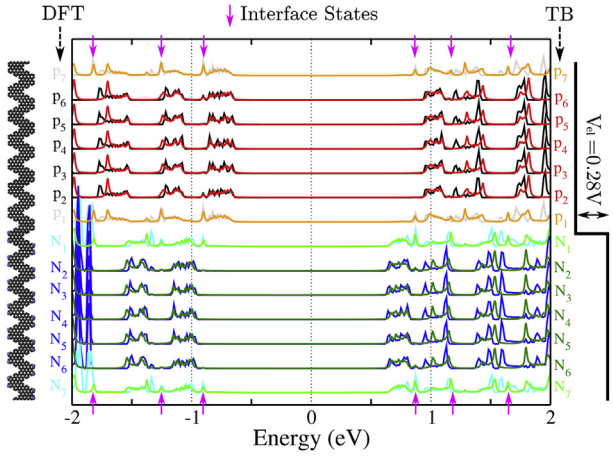

Fig. 2. Projected density of states (PDOS) of 7_{pristine} 7_{N2} GNW heterostructure. The PDOS is calculated with both DFT (VASP) and TB approaches in each of the 14 GNW unit cells labeled from p_1 (N_1) to p_7 (N_7) for the pristine (N2) unit cells. In case of the TB model, the electrostatic potential is calculated by introducing a constant electrostatic potential barrier of 0.28 V in the N2 GNW region. This reproduces well the DFT band offset generated in this heterostructure. (A colour version of this figure can be viewed online.)

We considered systems where either 20% or 40% of the pristine unit cells were substituted with the nitrogen rich ones. The DOS corresponding to these two disordered heterostructures is presented in Fig. 4 together with the DOS of the pristine GNW and the one of the N2 GNW shifted down by U_{el}. This manipulation facilitates the visualization of which part of the DOS originates from the pristine GNW, from the N2 GNW, or from both of them. In particular, one notes that the top valence states originate from the pristine GNW regions while the bottom conduction states are located in the N2 GNW regions as already noticed in the periodic heterojunction studied in Fig. 2.

We now focus on evaluating properties relevant to device design, using the real-space Kubo-Greenwood transport approach. These properties include the charge carrier mean free path (l_e), the charge carrier mobility (μ), the conductivity (σ), and the conductance (G). These quantities are deduced from the computation of the diffusivity ($D(t)$) which is related to the time evolution of the quadratic spreading of a wave packet ($\Delta\widehat{X}^2(t)$) along the transport direction (x). More details about the methodology are provided in the Method section and also in Refs. [37–40]. The transport properties (l_e, μ, G) obtained for the heterostructures of pristine GNW with random inclusions of N2 GNW segments are shown in Fig. 5.

4.1. Mean free path and mobility

All the scattering events in these heterostructures take place at or close to the interfaces, since transmission within the pristine and N2 regions is quasi-ballistic owing to the absence of intrinsic and extrinsic disorder. It is therefore expected that the length of the individual segments will determine the mean free path. Since the length of the N2 regions is restricted to the 8.5–27.3 nm range, the mean free path of the charge carriers contained in these regions should not vary, regardless of the N2-segment concentration. This scenario is precisely what we observe for the bottom conduction band electrons (Fig. 5, for energies in the 0.5–0.7 eV range). In contrast, the hole mean free path at the top valence band is strongly decreased when shifting from 80% pristine – 20% N2, to 60% pristine – 40% N2 since pristine segments are becoming shorter on average. This asymmetric behavior is also observed in the values of mobilities for charge carriers of opposite sign and for energies close to the band gap edges. The simulations indicate that the hole mobility is in the 550–150 cm^2 V^{-1} s^{-1} range, and the electron mobility is ~80 cm^2 V^{-1} s^{-1}. For charge carriers corresponding to the second group of valence and conduction states, mobilities are found in the range of 30–100 cm^2 V^{-1} s^{-1} and 50–250 cm^2 V^{-1} s^{-1}, respectively. We should recall that we only considered elastic coherent scattering, and these mobility values do not account for any possible electron-phonon scattering that would be present at finite temperature or for extrinsic source of scattering arising from the substrate for instance. Hence, the mobility values reported here should be considered as upper theoretical limits for random heterostructures made of pristine and N2 GNWs.

4.2. Conductance

We also present in Fig. 5 the electronic conductance in unit of $G_0 = 2\ e^2/h$ (the quantum of conductance). The Kubo-Greenwood conductance is obtained using the formula $G = \sigma/L$, where σ is the conductivity and L is usually the system length. In the Kubo-Greenwood formalism, L is however defined with respect to the propagation length as $2\sqrt{\Delta\widehat{X}^2(t)}$ [39–41], while $\sigma = \frac{e^2}{2}\rho \lim_{t\mapsto\infty} \frac{\partial\Delta\widehat{X}^2(t)}{\partial t}$. It should be realized that this definition differs from the more commonly used Landauer-Büttiker formula.

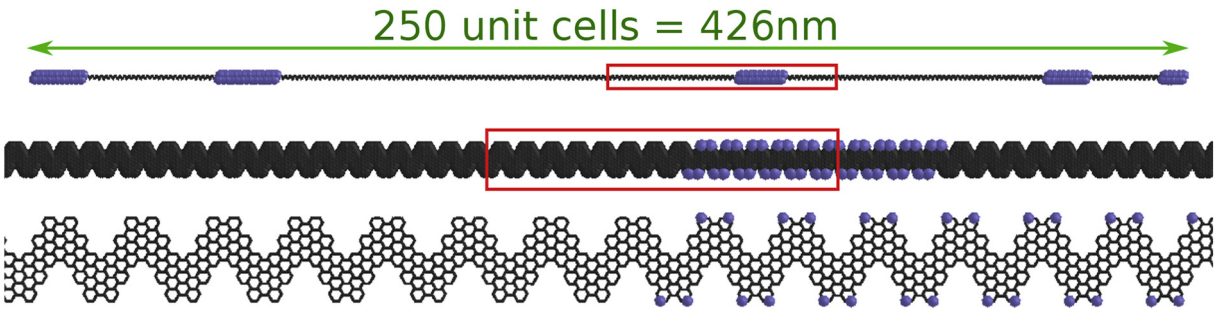

Fig. 3. A 426 nm long heterostructured GNW consisting of a pristine GNW with random inclusions of N2 GNW segments. The N2 regions are not only randomly placed but possess also a random length ∈[5 – 16] unit cells ([8.5 – 27.3] nm). The red box shows different levels of zoom-ins on the same area of the structure. (A colour version of this figure can be viewed online.)

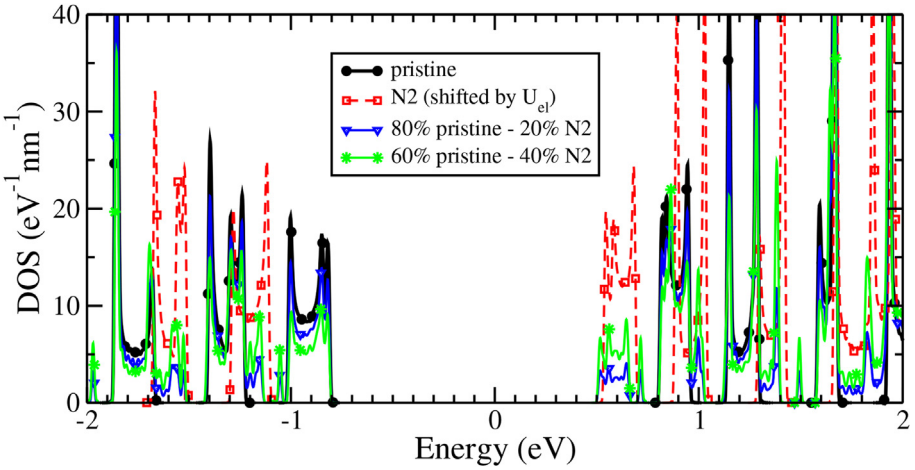

Fig. 4. Density of states (DOS) of different 1.7 μm long GNWs: A pristine GNW (black line with circle symbols), a N2 GNW (dashed red line with square symbols), a 80% pristine – 20% N2 heterostructured GNW (blue line with triangle symbols), and a 60% pristine – 40% N2 heterostructured GNW (green line with star symbols). The DOS of the N2 GNW is shifted by $U_{el} = -0.28$ eV.to account for the type II alignment. (A colour version of this figure can be viewed online.)

Indeed, in the Landauer picture, the conductance is given by the transmission probabilities from one side of the system to the other defining thus precisely the system length. When considering only elastic scattering mechanism, transmission is possible only if incoming and scattered states exist at the same energy. If the present 1.7 μm long heterostructured GNW is connected to source and drain electrodes, the Landauer-Büttiker conductance would therefore be dramatically reduced compared to the Kubo-Greenwood conductance. Indeed, the transmission will be zero for charge carriers at the bottom of conduction bands and at the top of valence bands because of the absence of a continuum of transmission channels. At these energies the holes and electrons are restricted to pristine and N2 regions respectively, and have therefore no possibility of traveling through the entire system. As a consequence, the transport gap should appear much larger than the actual electronic band gap. The calculated Kubo-Greenwood conductance should therefore be considered only at energies where both pristine and N2 regions contribute to the DOS. These energy windows are rather reduced and scarce as shown by filled purple regions in Fig. 5. It is therefore expected that this kind of heterostructure will poorly transmit electrical current [20]. The conductance plateaus defined by the purple regions in Fig. 5 represent the theoretical maximum conductance of the heterostructure considering a perfect transmission at interfaces. The Kubo-Greenwood conductance for two given lengths, i.e., $L = 20$ and 50 nm was computed for both heterostructures. Since the calculations were performed in the absence of contacts and that the Kubo-Greenwood formalism focuses on the diffusion properties rather than the transmission probabilities, a conductance can be computed for all energies. However, as explained above, these values are only meaningful in the purple regions of Fig. 5 since transmission will be zero elsewhere. For short lengths, such as $L = 20$ nm, the Kubo-Greenwood conductance can possibly predict higher than the theoretical maximum conductance depicted by the purple regions (e.g. at $E = +0.9$ eV) because it derives from the diffusion properties of both pristine and N2 GNW segments rather than transmission properties. However, the predicted properties are always lower than the maximum of the pristine and N2 segment alone as it should be (black line with circles and dashed red line with squares, respectively). For large enough lengths, the conductance will decrease because of increased number of scattering events, in reconciliation with Landauer picture. From this analysis, one can conclude that the conducting properties of contacted long pristine GNWs with random inclusions of N2 segments will be quite reduced although they exhibit interestingly high carrier mobilities inside a given segment.

5. Transport properties in a single junction between pristine and N2 AA-GNWs

Because the randomly doped heterostructures are predicted to have poor transmission properties, we now consider an alternative GNW configuration. The system is composed of a 1.7 μm long GNW, which is half pristine and half N2-doped. A single junction is present in the central part of the system (note that because of periodic conditions applied in the Kubo-Greenwood formalism, two junctions are needed to complete a unit cell and a second interface can

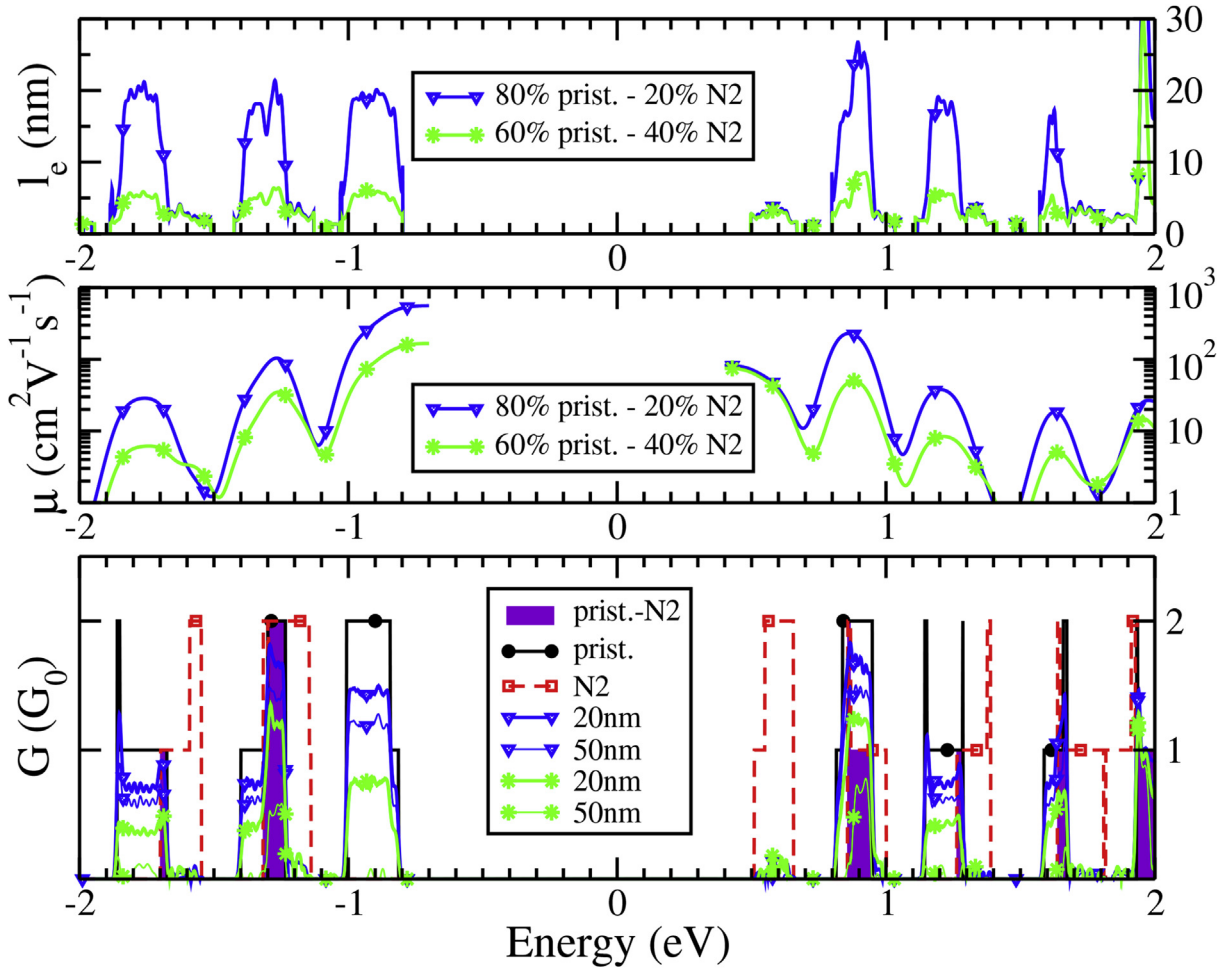

Fig. 5. Elastic mean free path (l_e), mobility (μ) and conductance (G) of 1.7 μm long heterostructured GNWs with two percentages of N2 regions (80% pristine − 20% N2, and 60% pristine − 40% N2). (A colour version of this figure can be viewed online.)

be found at the end of each segment). The mere presence of a junction guarantees that the issue related to poor transmission discussed in the previous section is still present. However, because scattering occurs only at one interface, the corresponding conductance should be close to the maximum theoretical value.

5.1. Substrate disorder

Since transport should be quasi-ballistic in each of the two individual regions, one should consider an extrinsic source of scattering to compute meaningful transport properties. Here a substrate was considered as such a source. The substrate used for transport measurements being typically silicon oxide, we here consider charged impurities trapped in the oxide as scattering centers. This type of disorder has been widely considered to assess transport properties of graphene (and other planar systems) [42–47]. Within the TB framework, this disorder potential operating on atomic site j is modeled by summing the contribution of the individual long range potential of all impurities (N_{imp}) located randomly in the substrate,

$$V_j = \sum_{i=1}^{N_{imp}} U_i \, e^{-\frac{|r_j - r_i|^2}{2\xi^2}} \quad (1)$$

with the individual impurity potential U_i chosen randomly in the range $-\Delta$ to $+\Delta$ and where ξ is the screening length. In the following the concentration of impurities ($C_{imp} = N_{imp}$/surface) is set to 10^{12} cm^{-2} and the screening length to 0.984 nm. The maximum impurity potential strength Δ is then varied using four values among {0.1,0.25,0.5,1.0} eV (see Fig. 6 for an example of the disorder potential). The transport properties for this system have been computed and averaged over six different realizations of a given disorder strength.

5.2. Mean free path and mobility

The calculated mean free paths and mobilities corresponding to this setup are presented in Fig. 7. For very weak disorder ($\Delta = 0.1$ eV), the mean free paths can possibly reach 100 nm, but the value rapidly reduces to 10 nm with increasing disorder strength to a still reasonable value of $\Delta = 1.0$ eV. This result tends to demonstrate that transport in such 1D GNWs will be quite sensitive to the substrate quality. Hence, similar to 2D graphene, a high-quality substrate, such as h-BN substrate, could be used to yield much better transport characteristic compared to silicon dioxide.

In spite of these issues, mobilities remain high, in the 10^2–10^3 cm^2 V^{-1} s^{-1} range for both holes and electrons. Again, this is only an upper limit, since the evaluation of these properties did not include scattering events such as non-elastic ones. The mean free path and mobilities values give an indication on how well electron (holes) can propagate in each of the 850 nm long pristine or N2 region, in the presence of substrate induced disorder. Eventually, although the transport properties appear to be sensitive to

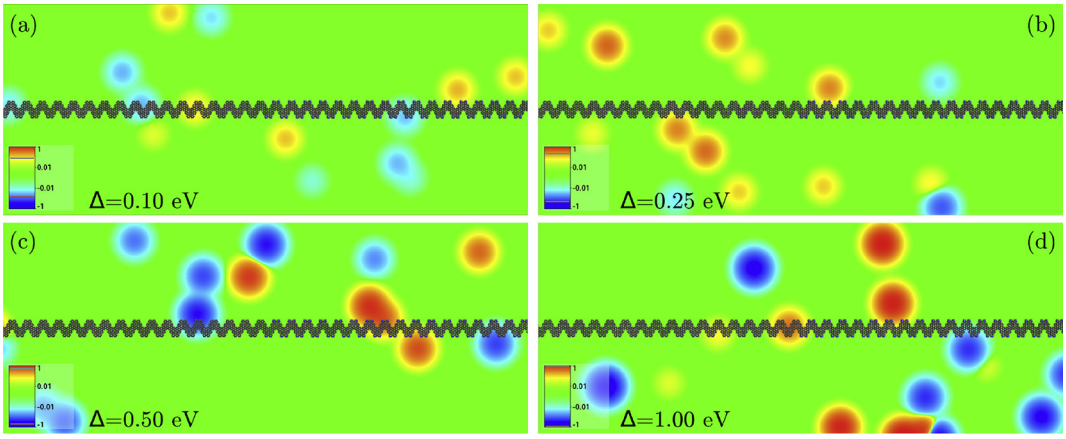

Fig. 6. Example of the disorder potential generated by a concentration of 10^{12} cm^{-2} of randomly positioned impurities following Equation (1) and with individual impurity strength randomly chosen in the interval [−Δ,+Δ]. Panels (a) to (d) correspond to Δ = 0.1, 0.25, 0.5, and 1 eV, respectively. (A colour version of this figure can be viewed online.)

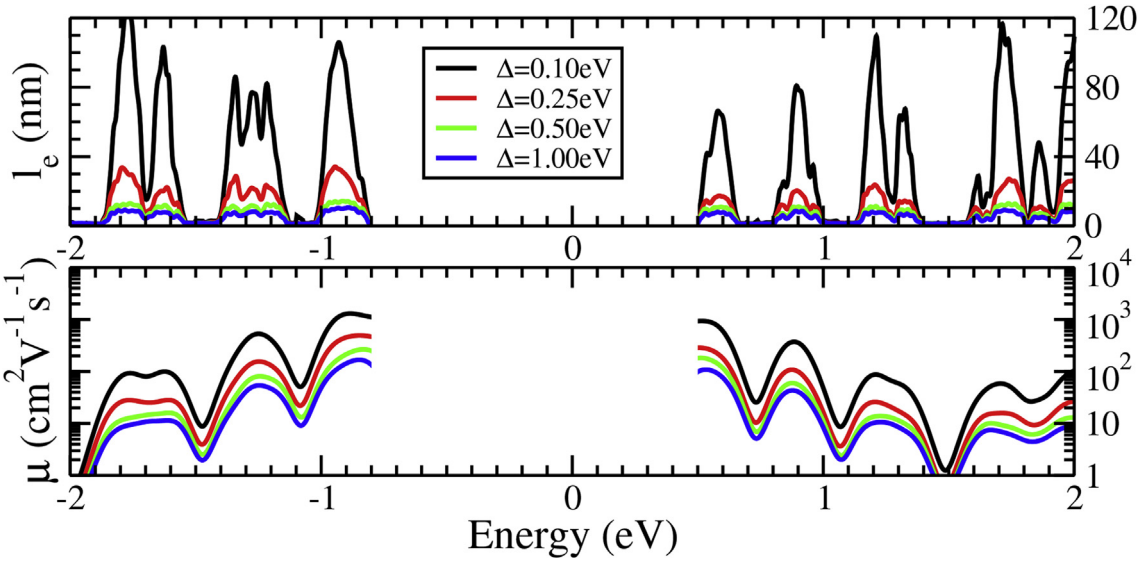

Fig. 7. Elastic mean free path (l_e), mobility (μ) of a 1.7 μm long pristine/N2 GNW heterojunction. (A colour version of this figure can be viewed online.)

substrate impurities, the reported mobilities indicate the great potential of such pristine-N2 GNW junctions as candidates for energy filters of charge carriers. This optimism comes from the fact that since transmission will be allowed for only small windows of energy (~ 25–90 meV) and that mobilities are maintained to high values, the heterojunctions considered here should efficiently select charge carriers of a given energy. This property is notably useful for selective energy contacts used to collect photo-generated hot carriers [48,49].

6. Discussion on the potential of GNW heterostructures for charge carrier separation devices

In this section, we discuss the possibility of using the two types of studied heterostructures for charge carrier separation applications. The interest now shifts from long range electrical transmission to charge separation capability. Since the DOS of holes and electrons in the two regions do not present a strong overlap, the junction has potential for charge separation and collection. By subjecting the materials to light, electron–hole pairs can be created. Note that the optical gap of the GNWs is smaller than the fundamental gap due to strong excitonic effects. For instance, according to a theoretical work [30] and a similar experimental study [33] by Fasel's group, the optical gap should be around 2.0 eV, i.e., in the visible range (~ 620 nm: yellow).

The presence of a staggered gap and the high electric field (~ 0.2 V nm^{-1}) at the interface should ease the separation of the photo-generated charges, showing that the advantage of this system is to avoid fast recombination of electron–hole pairs. Moreover, the absence of structural and edge defects should guarantee a good mobility (>100 cm^2 V^{-1} s^{-1} as presented in the previous section). This feature should make it easy to propagate and possibly collect photo-generated carriers once separated (for instance by applying a small bias potential). Using the pristine N2 single heterojunction architecture, a photoelectric current could thus be generated. However, even if the intensity of light absorption of such GNWs is important compared its monoatomic thickness (few percents), the stacking of several GNW heterojunctions would be required to absorb a greater amount of light as needed for instance for photovoltaic applications such as solar panels. However, stacking such heterostructures of varying width or dopant concentration could yield an efficient multi-junction design able to absorb photon

in a broad spectrum, since band gaps can change quasi continuously with these parameters [18,25]. The pristine N2 single heterojunction could presumably be suitable also for photo-detection of high sensitivity. Moreover, as discussed in the previous section such a GNW junction could also perform well as charge carrier energy filters.

The pristine GNW with random inclusions of N2 segments is predicted to have poor transmission capabilities. However, it might be well adapted for photocatalytic water splitting applications. The prototypical material for this application is TiO_2 which has a band gap of ~ 3 eV, and operates in the low UV spectrum. As discussed above, the bottom-up chemical synthesis ensures good crystallinity of both the channel and the interface, which is a key requirement for applications such as photocatalytic water splitting. Moreover, graphenic systems are usually rather chemically inert and should suffer much less from oxidation and corrosion issues compared to titania. An important property in the photocatalytic water splitting process is the rate of gas evolution of H_2 and O_2. This rate needs to be monitored with a preferred ratio of 2:1 [50]. This point could be addressed by using a GNW heterostructure containing twice as many segments for H_2 than the number used for O_2 production (see illustration in Fig. 8).

Another important point should be addressed to ensure an efficient photocatalytic water splitting process. The staggered type-II gap needs to be larger than 1.23 eV which corresponds to the redox energy couple required to convert water into molecular H_2 and O_2 [51]. Here, the calculated staggered gap is just slightly larger than this value, but it is also probably underestimated as it is usually the case with DFT. According to the recent experimental work on the pristine-N4 GNW heterojunction, the measured staggered gap is about 1.5 eV [20], satisfying this basic requirement. Furthermore, the staggered gap should preferentially straddle the energy levels of the redox reaction couple:

$$2\,H_2O + 4\,h^+ \rightarrow O_2 + 4\,H^+ (E \sim -5.73\ \text{eV}) \quad (2)$$

$$4\,H^+ + 4\,e^- \rightarrow 2\,H_2 (E \sim -4.50\ \text{eV}). \quad (3)$$

Therefore, the position of the staggered gap needs to be aligned with these two levels for water splitting, i.e. in the −5.73 to −4.5 eV range with respect to the vacuum level [52]. For the pristine GNW, the valence band maximum (VBM) and conduction band minimum (CBM) are −4.86 and −3.25 eV; for N2 GNW, the VBM and CBM are −5.22 and −3.60 eV; and for N4 GNW, the VBM and CBM are −5.42 and −3.91 eV. It follows that, for the pristine-N2 GNW junction, the bottom conduction band is located at −3.60 eV and the top valence band is at −4.86 eV. For the pristine-N4 GNW junction, the bottom conduction band is located at −3.91 eV and the top valence band is still at −4.86 eV. Unfortunately, these values do not fall into the −5.73 to −4.5 eV range. Note again that these numbers are obtained at DFT level for free-standing GNWs. Calculations of the work-function at the GW level usually down-shift these values by ~−0.5 eV. The substrate may also further down-shift everything to be within the −5.73 to −4.5 eV range. Alternatively, N2–N4 or N4–N6 GNW junctions can yield a better alignment since their work-function will be down-shifted. More careful studies are needed to assess integration of these heterojunctions into actual devices, but the possibility of tuning the work-function by changing the amount of nitrogen in GNW unit cell, and the possibility of tuning the concentration of N doped GNW segments to reach a 2:1 ratio and the atomically precise junction offer an interesting potential for photocatalytic water splitting applications.

7. Conclusion

We investigated the electronic and transport properties of pristine GNWs, N-doped GNWs, and their heterostructures, in configurations similar to those recently reported in the experimental study of Cai et al. [20]. We developed a tight-binding parametrization including a model of the electrostatic barrier generated at the interface between pristine and N-doped GNWs regions to study transport properties relevant to device design. Although mobilities are found to possibly be of the order of 1000 $cm^2\ V^{-1}\ s^{-1}$, the conductance properties across such GNW heterostructures are predicted to be largely reduced because of a misalignment of transmission channels. However, this particular misalignment allows for energy filtering of charge carriers, an interesting property for the design of selective energy contacts. Transport properties of a GNW heterostructure composed of a single junction were elucidated in the presence of substrate impurities as an extrinsic source of disorder. Reasonable large mobilities are predicted provided that the strength of the impurity potential remains low to moderate. This result demonstrates that as many other 1D systems, transport in GNW heterostructures is strongly sensitive to substrate disorder, further confirming that a rather clean substrate, such as h-BN should be employed to ensure

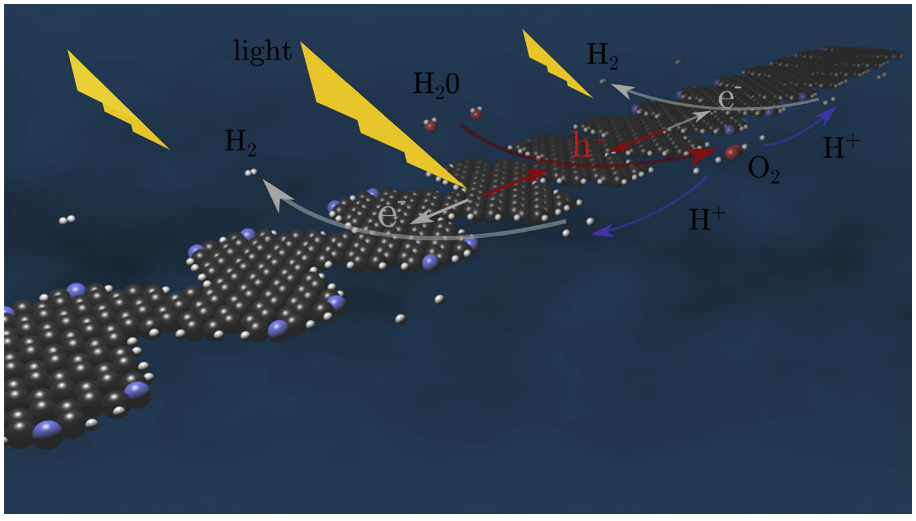

Fig. 8. Schematics of the photocatalytic water splitting process taking place at the junctions of a GNW heterostructure. (A colour version of this figure can be viewed online.)

good electronic transport properties. Further, we show that owing to the good mobilities, photo-created carriers should easily reach the junction and be blocked in its lowest energy region, i.e. the pristine (N-doped) region for holes (electrons). Although further investigations are needed to fully assess their behavior in actual device situations, this result indicates that the photo-generated carriers could be used for photo-detection and water splitting applications.

8. Methods

8.1. First principles calculations

The DFT calculations were conducted using either the VASP [27,28] or the SIESTA [26] package. Within the VASP calculations, plane-wave DFT calculations were carried out [27,28] within the generalized gradient approximation (GGA) implemented within the Perdew-Burke-Ernzerhof (PBE) exchange-correlation functional [53]. Atomic structures are relaxed until residual forces are below 0.02 eV/Å, using a fine k-point sampling mesh ($8 \times 1 \times 1$) within the Monkhorst-Pack scheme and projector augmented wave (PAW) pseudopotentials with a cutoff energy of 400 eV. A vacuum spacing of at least 14 Å in the non-periodic directions is enforced to avoid spurious interactions between periodic images in those directions. Within the SIESTA calculations, the PBE GGA functional [53] was employed. Core electrons were accounted for through the use of Troullier-Martins pseudopotentials [54]. The valence electron wavefunctions were expanded in a double-ζ polarized (DZP) basis set of finite-range numerical pseudoatomic orbitals [55]. The density was self-consistently calculated using a mesh cutoff of 250 Ryd and a $20 \times 1 \times 1$ ($8 \times 1 \times 1$) Monkhorst-Pack *k*-point grid [56] for the shorter (longer) systems. The atomic positions were optimized by relaxing the forces until a maximum tolerance criterion of 0.01 eV/Å is reached.

8.2. Tight-binding model

A semi-empirical single-band π–π^* TB model was developed to reproduce the DFT band structures of the pristine, type-N2 and type-N4 nitrogen doped GNW building blocks. In this model, the hopping terms up to the third nearest-neighbors are taken into account. The onsite and hopping terms of the edge carbon atoms have been modified to account for the hydrogenation. The onsite and hopping terms of the edge nitrogen atoms have also been parametrized in order to reproduce DFT results. The detailed parametrization of the present TB model is given in Table 1.

8.3. Kubo-Greenwood transport formalism

The transport properties were computed using the real-space Kubo-Greenwood approach. The propagation of wave packets is computed through the time-dependent Schrödinger equation by solving the time evolution operator $\widehat{U}(t) = e^{\frac{-i\widehat{H}t}{\hbar}}$ with an efficient Chebyshev polynomial method. It allows for computing associated time and energy dependent mean quadratic spreading (in a 1D system $\Delta\widehat{X}^2(E,t)$, $\widehat{X}$ being the position operator and the x-axis being the transport direction). The diffusivity is then evaluated directly from this quadratic spreading as $D(E,t) = \Delta\widehat{X}^2(E,t)/t$ with $\Delta\widehat{X}^2(E,t) = \frac{Tr[\delta(E-\widehat{H})|\widehat{X}(t)-\widehat{X}(0)|^2]}{Tr[\delta(E-\widehat{H})]}$, and with $\widehat{X}(t) = \widehat{U}(t)^{\dagger}\widehat{X}(0)\widehat{U}(t)$. Within the semi-classical picture, the diffusivity either increases linearly with time for ever in the ballistic limit when no scattering occur, or increases and then saturates to a maximal value D_{max} in the thermodynamic limit, i.e. after a large enough number of scattering events. However, in the quantum regime, interferences between scattering paths can possibly yield localization phenomena which cause a decrease in diffusivity. Eventually, for long enough propagation time, or equivalently for long enough propagation length, the diffusivity decreases exponentially and carriers enter the strong localization regime. The elastic mean free path l_e, the conductivity σ and the mobility μ discussed in the main text are semi-classical quantities deduced from the maximum of diffusivity curves (D_{max}) as $l_e = \frac{D_{max}}{2v}$ where v is the carrier velocity, $\sigma = \frac{e^2}{2}\rho D_{max}$ where e is the elementary charge and ρ is the density of states per length, and $\mu = \frac{\sigma}{n\,e}$ where n is the charge carrier density.

Table 1
Tight-binding parameters of the pristine and of the N-doped GNWs. Three species are accounted for in this model, one for the nitrogen atoms (*N*), and two for the carbons atoms, depending on whether they are edge atoms (C_2) or not (C_1). The onsite terms (ε) of each species is given first, followed by the hopping terms (γ). The interactions are considered up to the third nearest neighbors (γ_1,γ_2,γ_3). All the energy terms are given in eV. In this table, "*.*" denotes that this interaction is not observed in none of the three GNWs of the present study.

	Onsite terms		
	$\varepsilon(C_1)$	$\varepsilon(C_2)$	$\varepsilon(N)$
	0.00	0.60	−1.00
	Hopping terms		
Bond type	γ_1	γ_2	γ_3
C_1–C_1	−3.40	−0.25	−0.45
C_1–C_2	−3.30	−0.10	−0.30
C_1–N	−3.30	−0.10	−0.30
C_2–C_2	−2.75	0.10	−0.40
C_2–N	−3.50	0.10	−0.40
N–N	*.*	0.10	*.*

Acknowledgment

A.L. and J-C.C. acknowledge financial support from the F.R.S.-FNRS of Belgium, and from the Communauté Française de Belgique through the ARC on Graphene Nano-electromechanics (N 11/16-037). V.M. acknowledges the support from New York State under the New York State Office of Science, Technology and Academic Research (NYSTAR) Contract C080117 and the Office of Naval Research. L.L. was supported as a Eugene P. Wigner Fellow at Oak Ridge National Laboratory. Computational resources have been provided by the supercomputing facilities from the Université catholique de Louvain (CISM/UCL), from the Consortium des Equipements de Calcul Intensif en Fédération Wallonie Bruxelles (CECI), and from the Center for Computational Innovation at Rensselaer Polytechnic Institute (RPI). The authors declare no competing financial interests.

References

[1] K. Novoselov, A. Geim, S. Morozov, D. Jiang, Y. Zhang, S. Dubonos, et al., Electric field effect in atomically thin carbon films, Science 306 (5696) (2004) 666–669.
[2] A. Geim, Graphene: status and prospects, Science 324 (5934) (2009) 1530–1534.
[3] C. White, J.W. Mintmire, Density of states reflects diameter in nanotubes, Nature 394 (1998) 29–30.
[4] J.R. Sanchez-Valencia, T. Dienel, O. Gröning, I. Shorubalko, A. Mueller, M. Jansen, et al., Controlled synthesis of single-chirality carbon nanotubes, Nature 512 (7512) (2014) 61–64.
[5] Y. Son, M. Cohen, S. Louie, Energy gaps in graphene nanoribbons, Phys. Rev. Lett. 97 (21) (2006) 216803.
[6] P.A. Lee, T.V. Ramakrishnan, Disordered electronic systems, Rev. Mod. Phys. 57 (1985) 287–337.
[7] J. Cai, P. Ruffieux, R. Jaafar, M. Bieri, T. Braun, S. Blankenburg, et al., Atomically precise bottom-up fabrication of graphene nanoribbons, Nature 466 (7305) (2010) 470–473.

[8] J. Björk, S. Stafström, F. Hanke, Zipping up: cooperativity drives the synthesis of graphene nanoribbons, J. Am. Chem. Soc. 133 (38) (2011) 14884–14887.
[9] H. Huang, D. Wei, J. Sun, S.L. Wong, Y.P. Feng, A.H.C. Neto, et al., Spatially resolved electronic structures of atomically precise armchair graphene nanoribbons, Sci. Rep. 2 (2012).
[10] S. Linden, D. Zhong, A. Timmer, N. Aghdassi, J.H. Franke, H. Zhang, et al., Electronic structure of spatially aligned graphene nanoribbons on au(788), Phys. Rev. Lett. 108 (2012) 216801.
[11] T.H. Vo, M. Shekhirev, D.A. Kunkel, M.D. Morton, E. Berglund, L. Kong, et al., Large-scale solution synthesis of narrow graphene nanoribbons, Nat. Commun. 5 (3189) (2014).
[12] P. Han, K. Akagi, F. Federici Canova, H. Mutoh, S. Shiraki, K. Iwaya, et al., Bottom-up graphene-nanoribbon fabrication reveals chiral edges and enantioselectivity, ACS Nano 8 (9) (2014) 9181–9187.
[13] H. Sakaguchi, Y. Kawagoe, Y. Hirano, T. Iruka, M. Yano, T. Nakae, Width-controlled sub-nanometer graphene nanoribbon films synthesized by radical-polymerized chemical vapor deposition, Adv. Mater. 26 (24) (2014) 4134–4138.
[14] E. Costa Girão, L. Liang, E. Cruz-Silva, A.G.S. Filho, V. Meunier, Emergence of atypical properties in assembled graphene nanoribbons, Phys. Rev. Lett. 107 (2011) 135501.
[15] E. Costa Girão, E. Cruz-Silva, L. Liang, A.G.S. Filho, V. Meunier, Structural and electronic properties of graphitic nanowiggles, Phys. Rev. B 85 (2012) 235431.
[16] L. Liang, E. Cruz-Silva, E.C. Girão, V. Meunier, Enhanced thermoelectric figure of merit in assembled graphene nanoribbons, Phys. Rev. B 86 (2012) 115438.
[17] L. Liang, V. Meunier, Electronic and thermoelectric properties of assembled graphene nanoribbons with elastic strain and structural dislocation, Appl. Phys. Lett. 102 (14) (2013) 143101.
[18] C. Bronner, S. Stremlau, M. Gille, F. Brausse, A. Haase, S. Hecht, et al., Aligning the band gap of graphene nanoribbons by monomer doping, Angew. Chem. Int. Ed. 52 (16) (2013) 4422–4425.
[19] T.H. Vo, M. Shekhirev, D.A. Kunkel, F. Orange, M.J.-F. Guinel, A. Enders, et al., Bottom-up solution synthesis of narrow nitrogen-doped graphene nanoribbons, Chem. Commun. 50 (2014) 4172–4174.
[20] J. Cai, C.A. Pignedoli, L. Talirz, P. Ruffieux, H. Söde, L. Liang, et al., Graphene nanoribbon heterojunctions, Nat. Nanotech 9 (2014) 896–900.
[21] S. Yu, W. Zheng, C. Wang, Q. Jiang, Nitrogen/Boron doping position dependence of the electronic properties of a triangular graphene, ACS Nano 4 (12) (2010) 7619–7629.
[22] A. Lherbier, A.R. Botello-Méndez, J.-C. Charlier, Electronic and transport properties of unbalanced sublattice n-doping in graphene, Nano Lett. 13 (4) (2013) 1446–1450.
[23] J.R. Owens, E. Cruz-Silva, V. Meunier, Electronic structure and transport properties of n 2 aa -doped armchair and zigzag graphene nanoribbons, Nanotechnology 24 (23) (2013) 235701.
[24] P. Rani, V.K. Jindal, Designing band gap of graphene by b and n dopant atoms, RSC Adv. 3 (2013) 802–812.
[25] L. Liang, V. Meunier, Atomically precise graphene nanoribbon heterojunctions for excitonic solar cells, J. Phys. Chem. C 119 (1) (2015) 775–783.
[26] J.M. Soler, E. Artacho, J.D. Gale, A. García, J. Junquera, P. Ordejón, et al., The siesta method for ab initio order- n materials simulation, J. Phys.Condens. Matter 14 (11) (2002) 2745.
[27] G. Kresse, J. Furthmüller, Efficiency of ab-initio total energy calculations for metals and semiconductors using a plane-wave basis set, Comput. Mat. Sci. 6 (1) (1996) 15–50.
[28] G. Kresse, J. Furthmüller, Efficient iterative schemes for ab initio total-energy calculations using a plane-wave basis set, Phys. Rev. B 54 (16) (1996) 11169.
[29] L. Liang, V. Meunier, Electronic structure of assembled graphene nanoribbons: Substrate and many-body effects, Phys. Rev. B 86 (2012) 195404.
[30] S. Wang, J. Wang, Quasiparticle energies and optical excitations in chevron-type graphene nanoribbon, J. Phys. Chem. C 116 (18) (2012) 10193–10197.
[31] P. Ruffieux, J. Cai, N.C. Plumb, L. Patthey, D. Prezzi, A. Ferretti, et al., Electronic structure of atomically precise graphene nanoribbons, ACS Nano 6 (8) (2012) 6930–6935.
[32] L. Liang, E.C. Girão, V. Meunier, Quasiparticle band gaps of graphene nanowiggles and their magnetism on au(111), Phys. Rev. B 88 (2013) 035420.
[33] R. Denk, M. Hohage, P. Zeppenfeld, J. Cai, C.A. Pignedoli, H. Söde, et al., Exciton-dominated optical response of ultra-narrow graphene nanoribbons, Nat. Commun. 5 (2014) 4253.
[34] S.Y. Quek, L. Venkataraman, H.J. Choi, S.G. Louie, M.S. Hybertsen, J.B. Neaton, AmineGold linked single-molecule circuits: experiment and theory, Nano Lett. 7 (11) (2007) 3477–3482.
[35] B.G. Sumpter, L. Liang, A. Nicolaï, V. Meunier, Interfacial properties and design of functional energy materials, Acc. Chem. Res. 47 (0) (2014) 3395–3405.
[36] Y. Ma, Y. Dai, B. Huang, Realization of controlling the band alignment via atomic substitution, Carbon 69 (0) (2014) 495–501.
[37] D. Mayou, S.N. Khanna, A real-space approach to electronic transport, J. Phys. I Fr. 5 (9) (1995) 1199–1211.
[38] F. Triozon, J. Vidal, R. Mosseri, D. Mayou, Quantum dynamics in two- and three-dimensional quasiperiodic tilings, Phys. Rev. B 65 (2002) 220202.
[39] A. Lherbier, S.M.-M. Dubois, X. Declerck, Y.-M. Niquet, S. Roche, J.-C. Charlier, Transport properties of graphene containing structural defects, Phys. Rev. B 86 (2012) 075402.
[40] A. Uppstu, Z. Fan, A. Harju, Obtaining localization properties efficiently using the kubo-greenwood formalism, Phys. Rev. B 89 (2014) 075420.
[41] N. Leconte, A. Lherbier, F. Varchon, P. Ordejon, S. Roche, J.-C. Charlier, Quantum transport in chemically modified two-dimensional graphene: from minimal conductivity to anderson localization, Phys. Rev. B 84 (2011) 235420.
[42] K. Nomura, A.H. MacDonald, Quantum transport of massless dirac fermions, Phys. Rev. Lett. 98 (2007) 076602.
[43] J.H. Bardarson, J. Tworzydło, P.W. Brouwer, C.W.J. Beenakker, One-parameter scaling at the dirac point in graphene, Phys. Rev. Lett. 99 (2007) 106801.
[44] C.H. Lewenkopf, E.R. Mucciolo, A.H. Castro Neto, Numerical studies of conductivity and fano factor in disordered graphene, Phys. Rev. B 77 (2008) 081410.
[45] S. Adam, P.W. Brouwer, S. Das Sarma, Crossover from quantum to boltzmann transport in graphene, Phys. Rev. B 79 (2009) 201404.
[46] J.W. Kłos, A.A. Shylau, I.V. Zozoulenko, H. Xu, T. Heinzel, Transition from ballistic to diffusive behavior of graphene ribbons in the presence of warping and charged impurities, Phys. Rev. B 80 (2009) 245432.
[47] J.W. Kłos, I.V. Zozoulenko, Effect of short- and long-range scattering on the conductivity of graphene: Boltzmann approach vs tight-binding calculations, Phys. Rev. B 82 (2010) 081414.
[48] P. Würfel, Solar energy conversion with hot electrons from impact ionisation, Sol. Energy Mater. Sol. Cells 46 (1) (1997) 43–52.
[49] M.A. Green, Third generation photovoltaics: ultra-high conversion efficiency at low cost, Prog. Photovolt. Res. Appl. 9 (2) (2001) 123–135.
[50] L. Liao, Q. Zhang, Z. Su, Z. Zhao, Y. Wang, Y. Li, et al., Efficient solar water-splitting using a nanocrystalline coo photocatalyst, Nat. Nanotech. 9 (2014) 69–73.
[51] A. Kudo, Y. Miseki, Heterogeneous photocatalyst materials for water splitting, Chem. Soc. Rev. 38 (2009) 253–278.
[52] A.J. Nozik, R. Memming, Physical chemistry of semiconductor - liquid interfaces, J. Phys. Chem. 100 (31) (1996) 13061–13078.
[53] J.P. Perdew, K. Burke, M. Ernzerhof, Generalized gradient approximation made simple, Phys. Rev. Lett. 77 (1996) 3865–3868.
[54] N. Troullier, J.L. Martins, Efficient pseudopotentials for plane-wave calculations, Phys. Rev. B 43 (1991) 1993–2006.
[55] E. Artacho, D. Sánchez-Portal, P. Ordejón, A. García, J.M. Soler, Linear-scaling ab-initio calculations for large and complex systems, Phys. Status Solidi B 215 (1) (1999) 809–817.
[56] H.J. Monkhorst, J.D. Pack, Special points for brillouin-zone integrations, Phys. Rev. B 13 (1976) 5188–5192.